in P. Pasini, C. Zannoni and S. Zumer (editors),
Computer Simulations of Liquid Crystals and Polymers, Kluwer, Dordrecht (2005)

NEMATICS WITH DISPERSED POLYMER NETWORKS: FROM LATTICE SPIN MODELS TO EXPERIMENTAL OBSERVABLES

Cesare Chiccoli, Paolo Pasini
Istituto Nazionale di Fisica Nucleare, Sezione di Bologna,
Via Irnerio 46, I-40126, Bologna, ITALY
Paolo.Pasini@infn.bo.it

Gregor Skačej, Slobodan Žumer
Oddelek za fiziko, Univerza v Ljubljani,
Jadranska 19, SI-1000 Ljubljana, SLOVENIA
slobodan.zumer@fmf.uni-lj.si

Claudio Zannoni
Dip. di Chimica Fisica ed Inorganica, Università di Bologna,
Viale Risorgimento 4, I-40136, Bologna, ITALY
Claudio.Zannoni@cineca.it

Abstract We review our Monte Carlo studies of molecular ordering in nematic liquid crystals with dispersed polymer networks. Starting from the aligning effect of a single fiber, we study different network topographies and investigate regular and random arrays of straight and distorted polymer fibrils. We analyze the aligning ability of rough fibrils, external field-induced switching, and pretransitional ordering. The simulation output is used to calculate selected experimental observables: ^{2}H NMR spectra, capacitance, and intensity of transmitted polarized light.

Introduction

Polymer networks dispersed in liquid crystalline materials typically consist of thin fibers (few nanometers thick) or of somewhat thicker fiber bundles (see Fig. 1). Because of their high surface-to-volume ratio the polymer fibers can inuence orientational ordering of the sur-

rounding liquid crystal even at low polymer concentrations [1–3]. In this sense these dispersed systems are similar to "ordinary" confined systems where the liquid crystalline material is confined to microscopic cavities like droplets and pores. Apart from exhibiting a variety of interesting ordering- and confinement-related phenomena, liquid crystal-dispersed polymer networks are promising also for the construction of electrooptical devices based on the external field-induced switching process [4, 3]. The detailed characteristics of this process are closely linked to the anchoring and ordering conditions at the fiber surface, as well as to the shape and regularity of the network. Experimentally, these network properties can be regulated during the network formation (photopolymerization from the monomer-liquid crystal mixture) through various parameters: monomer solubility, curing temperature, ultra-violet (UV) light curing intensity, and the degree of orientational ordering in the liquid-crystalline component [1, 5, 6]. Similar types of network-like confinement can be achieved also in nematic-silica aerogel systems, where irregular chains of silica particles play the aligning role of polymer fibers [1]. While thin (nanometric) polymer fibers typically promote planar surface anchoring along the fiber direction, thicker fibers or fiber bundles (several tens of nm in diameter) can be treated with surfactants to yield homeotropic anchoring conditions.

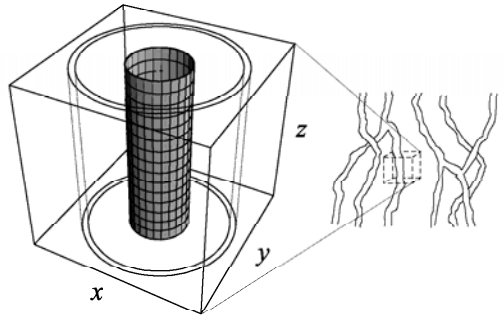

Figure 1. A sketch of the polymer network (*right*) and the simulation box with the cylindrical fiber and one of the cylindrical shells (*left*).

The existing experimental studies were usually accompanied by phenomenological (Landau-de Gennes-type) analyses [1, 2, 4, 3], but so far

almost nothing has been done for such network-like confinement at the microscopic level. For all these reasons here a thorough microscopic simulation study of the orientational coupling between polymer fibers and the surrounding liquid crystal will be presented. Like in the previous Chapter on PDLC droplets, the analysis will be based on the Lebwohl-Lasher (LL) lattice spin model [7], focusing on polymer networks with a well-defined average fiber direction, and on effects of roughness at the fiber surface [8]. Furthermore, for homeotropic anchoring, defects in nematic ordering due to topological constraints can be expected to form [9]. Their inner structure will be explored and compared with the existing phenomenological studies [10, 11]. Moreover, the simulations of switching in an external field will be presented and the role of network irregularities in switching characteristics (threshold etc.) will be examined [12]. Finally, paranematic surface-induced ordering above the bulk nematic-isotropic transition temperature will be explored in the system. For practical purposes, the simulation output will be expressed in terms of selected experimental observables: ^{2}H NMR spectra, electric capacitance, and transmitted intensity of polarized light.

In the LL model local orientations of close-packed nematic molecular clusters are represented by free unit rotors $\mathbf{u}_i$ (particles) attached to lattice points of a cubic lattice. The nearest neighbors $\mathbf{u}_i$ and $\mathbf{u}_j$ interact via

$$U_{ij} = -\epsilon \left[\frac{3}{2} (\mathbf{u}_i \cdot \mathbf{u}_j)^2 - \frac{1}{2} \right] \tag{1}$$

promoting parallel alignment, where $\epsilon \sim 0.02$ eV is the interaction strength. The boundary conditions are defined by fixing a set of "ghost" particles. Monte Carlo (MC) simulations are then employed to find equilibrium configurations, following the standard Metropolis scheme [13–15].

1. Aligning ability of the network

Consider a single straight cylindrical fiber oriented along the z-axis. The shape of the fiber can be defined by carving a jagged cylinder from the cubic lattice of the LL model and taking all particles that are lying closer than R — the fiber radius — from the center of the xy-plane (Fig. 1). The particle orientations in the surface layer of the fiber (ghost particles) are chosen in agreement with the desired boundary conditions and are kept fixed during the simulation. In the simulations reviewed here the strengths of nematic-nematic and nematic-ghost interactions were set equal, which corresponds to the strong anchoring limit. Further, periodic boundary conditions at the simulation box boundaries were

assumed. Such a set-up in fact corresponds to a regular array of straight and parallel fibers. Alternatively, if appropriately rescaled, it could also be interpreted as a colloidal crystal.

In the case of "perfect" anchoring ghost particle orientations were chosen either along $\mathbf{z}$ (a unit vector along the z-axis) for planar anchoring, or along the local radial unit vector for homeotropic anchoring. For rough fiber surfaces perfect planar or homeotropic ghost orientations were perturbed by additionally reorienting each of the ghost particles. The biasing distribution for this random reorientation was Gaussian in $\cos\theta$, where θ denotes the corresponding polar angle. The degree of randomness can be quantified by diagonalizing the ordering matrix $\underline{Q} = \frac{1}{2}(3\langle \mathbf{u}_i \otimes \mathbf{u}_i \rangle_g - \mathbf{l})$ (the average $\langle ... \rangle_g$ taken over ghosts), which gives the ghost director and the corresponding order parameter $\langle P_2 \rangle_g$. In all cases the $\langle P_2 \rangle_g$ order parameter is referred to the z-axis, the fiber direction. Hence, $\langle P_2 \rangle_g = 1$ and $\langle P_2 \rangle_g = -0.5$ correspond to perfect planar and homeotropic alignment, respectively, while intermediate (but nonzero) values correspond to partial order on the boundary surface.

The simulation box size was set to $30a \times 30a \times 30a$, which for the chosen fiber radius ($R = 5a$, a denoting the lattice spacing) amounts to 24600 nematic and 840 ghost particles in total. The simulation box side is larger than the nematic correlation length ($< 5a$ in the temperature range studied), which is enough to avoid artifacts in ordering due to periodic boundary conditions. Simulation runs were started from a completely random (isotropic) orientational configuration not to impose any preferred orientation in the system. Once the system was equilibrated (after at least 6×10^4 MC cycles), a sequence of 6.6×10^4 (or more) successive particle configurations was used to calculate relevant observables, including ^{2}H NMR spectra following the methodology presented in the preceding Chapter.

To quantify the degree of ordering with respect to $\mathbf{z}$, it is convenient to calculate the radial dependence of $\langle P_2^z \rangle = \frac{1}{2}\left[3\langle (\mathbf{u}_i \cdot \mathbf{z})^2 \rangle_r - 1\right]$. The average $\langle ... \rangle_r$ has to be performed over all nematic particles $\mathbf{u}_i$ belonging to the cylindrical layer with radius r (see Fig. 1), and over MC cycles. Neglecting significant collective molecular reorientation during the MC evolution, it is instructive to calculate also spatially-resolved director and order parameter maps $\mathbf{n}(\mathbf{r}_i)$ and $S(\mathbf{r}_i)$, respectively, where $\mathbf{r}_i$ denotes the position of the ith lattice site. For this purpose the local ordering matrix $\underline{Q}(\mathbf{r}_i) = \frac{1}{2}(3\langle \mathbf{u}_i \otimes \mathbf{u}_i \rangle_{\mathbf{r}_i} - \mathbf{l})$ was averaged over MC cycles and then diagonalized, yielding the local value of the order parameter $S(\mathbf{r}_i)$ and the corresponding eigenvector — the local director $\mathbf{n}(\mathbf{r}_i)$. Similarly, the biaxiality map $P(\mathbf{r}_i)$ can also be deduced from the data.

1.1 Planar anchoring

First consider a nematic sample at $T^* = k_BT/\epsilon = 1.0$, with planar anchoring along the z-axis and with possible deviations from this perfect alignment, as described above. The $\langle P_2^z \rangle$ curves shown in Fig. 2 (a) correspond to a series of polymer fibers whose surface morphology varies from smooth to rough and disordered, that is from $\langle P_2 \rangle_g = 1$ to $\langle P_2 \rangle_g \approx 0$. For perfect planar anchoring $\|\mathbf{z}$ the nematic director $\mathbf{n}$ is parallel to $\mathbf{z}$. In this case $\langle P_2^z \rangle$ becomes a direct measure for S, the standard nematic order parameter, because $\mathbf{n}$ and $\mathbf{z}$ coincide. Far enough from the fiber the value of $\langle P_2^z \rangle$ approaches ≈ 0.6, matching with that of S in a bulk sample at $T^* = 1.0$ [16], while close to the fiber there is an increase in $\langle P_2^z \rangle$, reflecting the fiber-induced enhancement of nematic order. The characteristic length of the nematic order variation at the given T^* roughly amounts to $\approx 3a$.

Studying cases with reduced (imperfect) planar anchoring $\|\mathbf{z}$ [Fig. 2(a)], one can see that at least down to $\langle P_2 \rangle_g \approx 0.25$ the bulk value of $\langle P_2^z \rangle$ parameters remains essentially unchanged if compared to the perfect $\langle P_2 \rangle_g = 1$ case. Note that now for, e.g., $\langle P_2 \rangle_g \approx 0.75$ the increase of order close to the fiber is smaller than for $\langle P_2 \rangle_g = 1$, and that already for $\langle P_2 \rangle_g \approx 0.50$ (as well as for $\langle P_2 \rangle_g \approx 0.25$) the surface degree of order is somewhat lower than its bulk value. From these observations one can conclude that the first effect of the partial disorder in surface anchoring is merely a slight decrease in the degree of nematic order in the vicinity of the fiber, but that at this point the long-range orienting ability of the polymer network is not lost. This ability, however, weakens upon further decreasing $\langle P_2 \rangle_g$, but is present at least down to $\langle P_2 \rangle_g \approx 0.09$ (the corresponding profiles not plotted here). Then only in a sample with a completely disordering fiber — for $\langle P_2 \rangle_g \approx 0$ — the net orientation of the nematic for the LL intermolecular potential is completely independent of the fiber direction. This follows from the behavior of the $\langle P_2^z \rangle$ order parameter which now can take any arbitrary value, and from the fact that the liquid crystal is still nematic, as suggested by a nonzero value of the S order parameter throughout the sample. Note that the bulk value of S remains almost unaltered in comparison with, e.g., the $\langle P_2 \rangle_g = 1$ case. The fact that it is actually slightly lower than the value obtained for $\langle P_2 \rangle_g = 1$ (≈ 0.6) can be attributed to slow collective molecular motion during the production run.

If temperature in the LL model is increased to $T^* = 1.2$, in a bulk sample the isotropic phase is stable — recall that the nematic-isotropic (NI) transition takes place at $T^*_{NI} = 1.1232$ [16]. However, like in PDLC droplets, also in the vicinity of polymer fibers one should expect

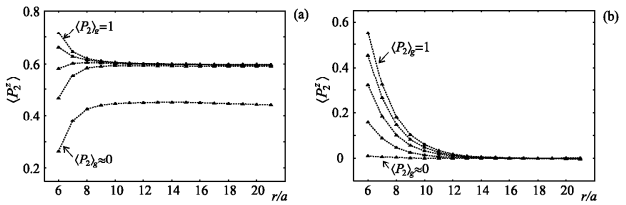

Figure 2. Order parameter $\langle P_2^z \rangle$ versus r (the distance from the simulation box center, measured in lattice units a) in a sample containing a single cylindrical fiber with $R = 5a$. Planar anchoring along the z-axis; (a) nematic ($T^* = 1.0$) and (b) isotropic phase ($T^* = 1.2$). In the plots each of the curves corresponds to a different degree of ordering in the ghost particle system: $\langle P_2 \rangle_g \approx 1.0$, 0.75, 0.50, 0.25, and 0 (top to bottom).

surface-induced paranematic ordering. For the case of planar anchoring $\|\mathbf{z}$ Fig. 2 (b) shows $\langle P_2^z \rangle$ profiles (coinciding with S profiles) and in fact confirms the existence of surface-induced planar ordering. The net molecular orientation is still along $\mathbf{z}$, as imposed by the fiber, and the corresponding degree of order decays to zero over a characteristic length of the order of $\xi \approx 5a$.

1.2 Homeotropic anchoring: topological defects

Proceeding now to cases with $\langle P_2 \rangle_g < 0$, i.e., to perturbed homeotropic ordering, already for $\langle P_2 \rangle_g \approx -0.08$ the polymer fiber is able to align the liquid crystal. Molecules are now aligned perpendicular to $\mathbf{z}$, the fiber direction, i.e., mainly within the xy-plane, which yields $\langle P_2^z \rangle < 0$ for all r. The most interesting case, however, is the one with perfect homeotropic anchoring. In this case the radial alignment promoted by the fiber requires formation of topological defects in nematic ordering in order to satisfy periodic boundary conditions. As shown in the director map $\mathbf{n}(\mathbf{r}_i)$ (Fig. 3, left), a pair of $-\frac{1}{2}$ strength defect lines forms along the fiber and close to the simulation box diagonal.

As concluded from topological considerations (conservation of topological charge) either a -1 strength disclination line or a pair of $-\frac{1}{2}$ lines can form in the neighborhood of a homeotropic fiber, and this is seen also in simulation. The -1 line, however, does not seem to be stable and splits into a pair of $-\frac{1}{2}$ lines during the MC evolution, even if it is taken as initial configuration in the simulation run. This agrees with simple

estimates of defect line free energy where the this energy scales as m^2 (where m is the defect strength) [17, 18]. Moreover, a stable "escaped" structure (bent in the **z**-direction) could not be observed in the present simulations. Note that the defects are able to form because anchoring is rather strong and that for weaker nematic-ghost interaction strength (or, alternatively, a disordered fiber surface) they vanish. The following analysis is relevant not only for fiber network systems, but also for elongated colloidal particles embedded in a liquid crystal host [9].

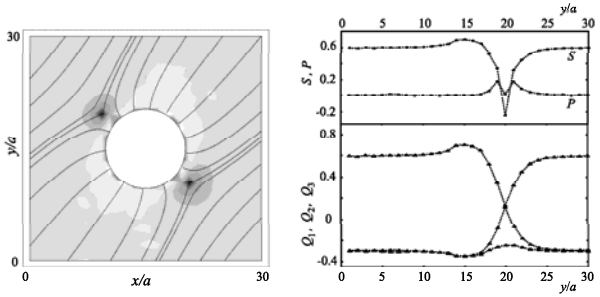

Figure 3. *Left:* cross section of the director field $\mathbf{n}(x, y)$ represented by "streamlines". The shading represents the value of the order parameter $S(x, y)$ (dark values correspond to low S). A pair of $-\frac{1}{2}$ defects has formed on the diagonal. In the defect core molecules are (on the average) aligned in the xy-plane; ordering is uniaxial with $S < 0$ and the corresponding eigenvector, $\mathbf{n}$, is directed out of plane (along the z-axis). *Right:* eigenvalues of the ordering matrix Q_1, Q_2, and Q_3 plotted across the left defect along the y axis. In the upper panel the order parameter S and biaxiality P are plotted. The left-right asymmetry with respect to the defect core positioned at $y/a = 20$ is due to the presence of the fiber. While S exhibits a simple decrease if the defect is approached from any direction, P shows a more complex crater-like profile.

In our simulations, the defect line pair always forms close to one of the simulation box diagonals although the cross section of the fiber is axially symmetric (ignoring its jagged shape). This symmetry breaking may be attributed to the repulsion between defects maximizing the defect-to-defect distance (recall the periodic boundary conditions), and to a finite-size effect originating from collective fluctuations, resulting in a tendency to align the nematic director along the simulation box diagonal. Further, with increasing temperature, as well as with increasing fiber radius, the defects move away from the fiber surface [8]. The actual locus of defect

lines is determined by the subtle interplay between curvature elasticity and nematic-to-isotropic melting inside the defect core.

The inner structure of a defect line is characterized by variations in the three eigenvalues of the local ordering matrix $\underline{Q}(\mathbf{r}_i)$, Q_1, Q_2, and Q_3. The eigenvalues, along with the corresponding eigenvectors, were obtained by diagonalizing $\underline{Q}(\mathbf{r}_i)$ for each of the lattice sites. The scalar order parameter S, biaxiality P, and director $\mathbf{n}$ maps can be derived from these data, as discussed earlier. Fig. 3 (left) shows the director field and the order parameter map in the plane perpendicular to the long axis of the fiber. Fig. 3 (right) shows the Q_1, Q_2, and Q_3-profiles plotted along the y-axis through the left of the two disclinations. After passing through the disclination, the Q_1 and Q_2 components change sign. Moreover, their positive values are roughly equal to twice the magnitude of the negative ones, which is attributed to the director rotation by approximately $\pi/2$ when one crosses the defect along the y axis (the orientation of the eigensystem changes continuously on passing through the defect). On the other hand, the Q_3-component does not change significantly, indicating that the variation in the nematic ordering mostly occurs in the xy-plane perpendicular to the fiber direction, **z**.

Alternatively, the Q_1, Q_2, and Q_3-profiles can be interpreted also in terms of order parameters S and P (see Fig. 3, right), and the molecular ordering close to a disclination line can be summarized as follows. In the very center of the defect molecular ordering is uniaxial with $S < 0$ and $P \to 0$. Far enough from the defect line the nematic liquid crystal is uniaxial, too, however, with $S > 0$ and $P = 0$, as expected in a homogeneous or in a weakly distorted bulk sample. In the intermediate ring-like region, nematic ordering is biaxial with $P \neq 0$. These conclusions agree also with results from alignment tensor-based phenomenological analyses of topological defects both of half-integer [10] and integer strength [11].

1.3 ^{2}H NMR spectra

The observations regarding the aligning ability of the fiber can be confirmed also by calculating ^{2}H NMR spectra using the numerical output from MC simulations. The quadrupolar line splitting

$$\omega_Q(\mathbf{r}) = \pm\delta\omega_Q S(\mathbf{r}) \left[\frac{3}{2}\cos^2\theta(\mathbf{r}) - \frac{1}{2}\right] \qquad (2)$$

depends on the angle $\theta(\mathbf{r})$ between the local director and the magnetic field of the NMR spectrometer, as well as on the local degree of order $S(\mathbf{r})$, with $\delta\omega_Q \approx 100$ kHz. Fig. 4 shows the NMR spectra calculated in the nematic (left, $T^* = 1.0$) and in the isotropic phase (right, $T^* = 1.2$),

with the NMR spectrometer field applied along the fiber direction **z**. The calculation was based on generating the relaxation function $G(t)$ from the MC data and calculating its Fourier transform representing the spectrum. In this way also effects of homogeneous translational diffusion were included. Following the methodology applied in the previous Chapter to PDLC droplets [19], the diffusive molecular motion was simulated by a random walk on the cubic lattice, performing 1024 diffusion steps per NMR cycle. The effective diffusion constant for such a random-walk process can be estimated to be $D = 256a^2\delta\omega_Q/3\pi$, yielding a root-mean-square molecular displacement of $\sqrt{6Dt_0} = 32a$ in each NMR cycle. Here $t_0 = 2\pi/\delta\omega_Q$ denotes the NMR cycle duration, while $\delta\omega_Q$ is the quadrupolar splitting. Since this displacement is comparable to the sample size, the calculated NMR spectra are expected to be highly diffusion-averaged. Note that nematic particle configurations were updated 1024 times per NMR cycle — thereby matching with the natural time scale for fluctuations of molecular long axes. For smoothing purposes, a convolution of the spectra with a Lorentzian kernel of width $\approx 0.07\,\delta\omega_Q$ was performed. Finally, note that the NMR spectrometer magnetic field is assumed to be weak enough not to align nematic molecules which indeed is the case for strongly confined systems.

The calculated spectra are shown in Fig. 4. In the nematic phase with perfect planar anchoring ($\langle P_2\rangle_g = 1$) in the spectrum one has two peaks positioned at $\omega_Q/\delta\omega_Q \approx \pm 0.6$. In the chosen geometry, $|\omega_Q/\delta\omega_Q|$ is supposed to be roughly equal to the value of S, the nematic order parameter, since the director and the direction of the NMR spectrometer magnetic field coincide. Indeed, for $T^* = 1.0$ one finds $S \approx 0.6$. Translational diffusion in this case affects the spectra only negligibly: the nematic director is homogeneous throughout the sample and the degree of order is enhanced only slightly in the vicinity of the fiber. Therefore, the effect of diffusion should be merely a slight increase in quadrupolar splitting, but the resolution of the spectra is not high enough to clearly see this surface ordering-induced shift.

Proceeding now to fibers with partially disordered anchoring, in the spectra there is no noticeable change at least down to $\langle P_2\rangle_g \approx 0.25$, reflecting the ability of the polymer network to align the surrounding liquid crystal along **z**. In the case when anchoring is completely disordered with $\langle P_2\rangle_g \approx 0$, the spectrum typically still consists of two peaks, however, the corresponding splitting can be arbitrary because there is no preferred direction in the system — note that only one of the possible spectra is plotted. Note also that sometimes during the acquisition of the $G(t)$ signal slow collective molecular motion can occur, which results in an increase of the spectral line width. On the other hand, in

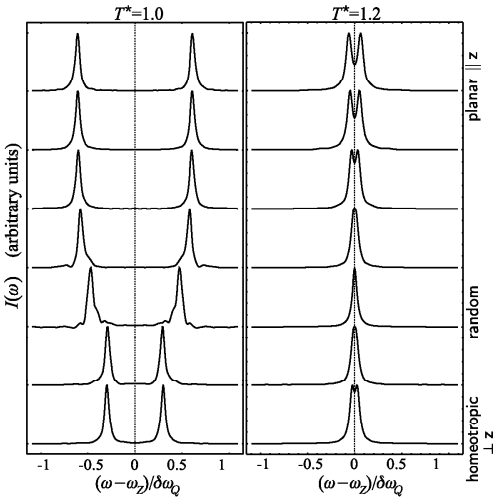

Figure 4. ^{2}H NMR spectra; $T^* = 1.0$ (*left*) and $T^* = 1.2$ (*right*). Top to bottom: spectra for $\langle P_2\rangle_g$=1.0 (planar), 0.75, 0.5, 0.25, 0 (random), −0.25, and −0.5 (homeotropic). The aligning capability of the network is lost only for $\langle P_2\rangle_g \approx 0$. ω_Z stands for the Zeeman frequency (also elsewhere).

homeotropic cases with $\langle P_2\rangle_g < 0$, molecular ordering is confined to the xy-plane. The quadrupolar splitting now decreases by 50% with respect to perfect planar anchoring because the director is perpendicular to the spectrometer field direction (see the two spectra in the bottom of Fig. 4, left).

In the bulk isotropic phase, however, quadrupolar interactions giving rise to the ω_Q splitting are averaged out by the rapid molecular motion. Therefore, ignoring translational diffusion, in a confined system for $S \approx 0$ one should expect a single-peaked spectrum at $\omega_Q \approx 0$, somewhat broadened by the surface-induced order. The spectra shown in Fig. 4, right, were calculated assuming fast translational diffusion, and it is evident that some of them are actually double-peaked. This is a clear signature of surface-induced paranematic order. In fact, the peak-to-peak distance decreases with decreasing degree of surface order; compare

with Fig. 2 (b). For $\langle P_2 \rangle_g \approx 0$ exhibiting no surface order, the spectrum is again single-peaked. Again, the splitting observed for perfect planar anchoring roughly amounts to twice the splitting seen in the perfectly homeotropic case.

2. External field-induced switching

This Section is going to address the external field-induced switching of the molecular orientation in a nematic with dispersed polymer networks. First a regular array of straight and parallel polymer fibers will be treated, like in aligning ability studies, assuming perfect planar anchoring. Then we will proceed to more complex network topographies, with irregularities in fiber positions. At the end, a system of distorted and cross-linked fibers will be treated. In all cases the fiber surface will be assumed smooth, with planar anchoring along the local fiber direction. The switching process will be monitored by inspecting selected experimental observables predicted from the simulation output.

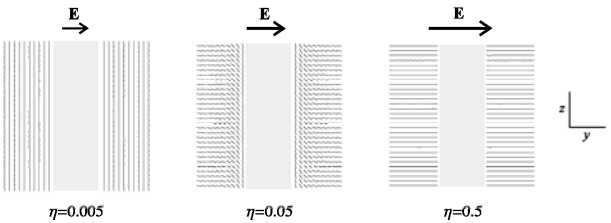

Figure 5. Switching in a regular fiber array: examples of director fields for different $\eta \propto E^2$; $T^* = 1.0$, $R = 5a$, and $w = 1$ (yz-cross sections through the fiber center). From left to right: homogeneous (h), deformed (d), and saturated (s) structure. Anchoring easy axis is planar and $\|\mathbf{z}$, while the external field $\mathbf{E}$ is directed along $\mathbf{y}$. Note that the d-structure is twisted along the x-axis, while there is no twist in a simple nematic slab. This, however, does not affect the qualitative analogy of the two systems.

2.1 Regular fiber array

Let the fiber direction coincide with $\mathbf{z}$, as shown in Fig. 1. An external field applied perpendicular to the fibers (e.g., along the y-axis) creates a conflict between the aligning tendencies of the fiber array and of the field; see Fig. 5 (a). Note that switching experiments are usually

performed in an external electric field, which in anisotropic dielectric materials requires Maxwell equations to be solved in order to obtain the local electric field strength $\mathbf{E}$. For simplicity, however, in the following $\mathbf{E}$ will be assumed homogeneous. Alternatively, one could perform a switching experiment also in an external magnetic field where the inhomogeneities of the corresponding susceptibility are weaker, making the field homogeneity assumption more plausible. In the LL model the field contribution to the Hamiltonian for each particle is given by

$$U_i^f = -\epsilon\eta \left[\frac{3}{2} (\mathbf{u}_i \cdot \mathbf{f})^2 - \frac{1}{2} \right], \tag{3}$$

where η is proportional to the square of the external field strength and $\mathbf{f}$ is a unit vector in the field direction. Finally, the switching threshold is sensitive to changes in the surface anchoring strength. Therefore, here cases with different anchoring strengths will be examined, with a dimensionless anchoring strength defined as $w = \epsilon_g/\epsilon$. Here ϵ_g denotes the nematic-ghost interaction strength and ϵ the nematic-nematic one.

The possible director configurations in a regular fiber array sample (Fig. 5) are equivalent to those encountered in a simple nematic slab. Imagine a slab of thickness d sandwiched between two parallel plates imposing strong planar anchoring along the z-axis, and let there be an external field $\mathbf{f}$ applied along the slab normal (y-axis). In a weak external field the equilibrium director profile is homogeneous with $\mathbf{n} \perp \mathbf{f}$ ("h-structure"). Increasing the field strength E, at first the director profile does not change, but once the Fréedericksz threshold $E_F^0 \propto d^{-1}$ is reached, a transition to a deformed structure is observed ("d-structure"). For finite anchoring strengths W the Fréedericksz threshold E_F is somewhat reduced [20]. Increasing the field strength even further, for finite W the orienting effect of the field overwhelms the anchoring and a second, saturation transition takes place. Above this second threshold E_s nematic molecules are aligned uniformly along the field, with $\mathbf{n}\|\mathbf{f}$ ("s-structure"). Note that in case of weak anchoring or in a very thin nematic slab with $K/W \gg d$ (K standing for the Frank elastic constant), the thresholds E_F and E_s attain similar values, indicating that the region of stability for the deformed d-structure becomes extremely narrow [20].

In the MC simulation, the sample size was again set to $30a \times 30a \times 30a$ and the fiber radius to $R = 5a$. All simulations were performed at $T^* = 1.0$, deep in the nematic phase. To reliably estimate the field thresholds for the Fréedericksz and saturation transitions from the MC simulation, external field strength scans were performed for a given anchoring strength w by gradually increasing/decreasing the field strength.

Since orientational fluctuations can increase significantly in the vicinity of structural transitions, rather long equilibration and production runs (1.2×10^5 MC cycles each) were necessary to produce reliable results.

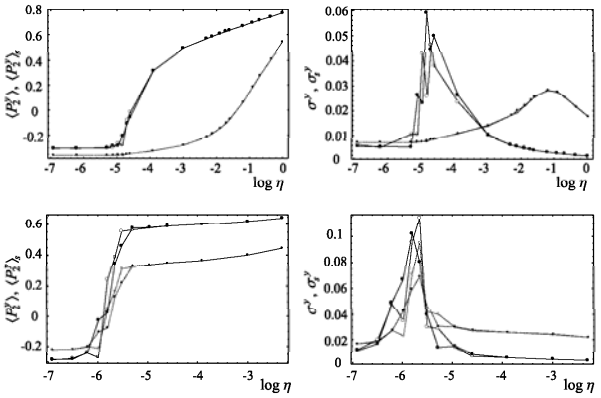

Figure 6. Order parameters $\langle P_2^y \rangle$ (solid line) and $\langle P_2^y \rangle_s$ (dotted line), plus the corresponding variances σ^y and σ_s^y. *Top:* strong anchoring ($w = 1$), *bottom:* weak anchoring ($w = 0.1$). Closed circles correspond to scans upon increasing η, the open ones to scans upon decreasing. Fréedericksz and saturation thresholds can be deduced from the positions of the σ^y and σ_s^y peaks, respectively. For $w = 0.1$ both transitions virtually overlap.

A suitable order parameter for monitoring the Fréedericksz transition (involving a significant number of nematic particles) is $\langle P_2^y \rangle = \frac{1}{2}\langle 3(\mathbf{u}_i \cdot \mathbf{y})^2 - 1 \rangle$, where the average $\langle ... \rangle$ is performed over all particles and MC cycles, and $\mathbf{y}$ represents a unit vector along the field direction. If, on the other hand, the average $\langle ... \rangle$ is taken over particles in the first layer next to the fiber only (of thickness a), one obtains $\langle P_2^y \rangle_s$ that is sensitive to the subsurface reorientations characteristic for the saturation transition. The sudden increase either of $\langle P_2^y \rangle$ or $\langle P_2^y \rangle_s$ is accompanied by a significant increase of fluctuations of these order parameters. Therefore, the corresponding variances σ^y and σ_s^y can be used to accurately determine the position of the threshold for both transitions.

For $w = 0.1$ and $w = 1$ the behavior of $\langle P_2^y \rangle$ and $\langle P_2^y \rangle_s$ upon increasing field strength, along with their variances, is shown in Fig. 6. Note that the reproducibility of the data points is good (comparing scans up and down in field strength), yet it is somewhat poorer in the $w = 0.1$ case where the surface anchoring is much weaker than for $w = 1$. The fact that there is no obvious hysteresis suggests that both the Fréedericksz and the saturation structural transitions are second-order (hence continuous), in agreement with phenomenological studies.

The threshold values for both transition types at different values of anchoring strength are summarized in a structural phase diagram. For $T^* = 1.0$ and $R = 5a$ it is shown in Fig. 7, together with the equivalent phase diagram for a nematic slab, derived phenomenologically in Ref. [20]. In weak enough fields one can always find the h-structure, while in strong enough fields the s-structure is always seen. The d-structure appears at intermediate field strengths, but its stability region gets narrower with decreasing w. As shown in Ref. [20] for the case of a nematic slab, the h-d and d-s coexistence lines do not merge upon decreasing the anchoring strength and there is no triple point where all three structures would coexist. Due to finite accuracy of field threshold estimates, in the present stability analysis the Fréedericksz and saturation transitions below a certain anchoring strength ($w \approx 0.1$) coalesce and cannot be distinguished anymore. Note that the qualitative agreement with the phase diagram for the nematic slab [20] is rather good. Preliminary tests show that the coexistence lines in the diagram are essentially insensitive to changing T^*.

The position of the h-d coexistence line corresponding to the Fréedericksz transition is expected to depend on the effective fiber-to-fiber distance d_*: with decreasing d_* at fixed w and T^* the line is expected to move towards higher critical field strengths. On the other hand, the d-s saturation transition line should not shift significantly. To check these statements, one can explore transitions in a network consisting of somewhat thinner fibers. Setting $R/a = 3$ (instead of $R/a = 5$ above) and considering a $18 \times 18 \times 18$ sample with a single fiber (instead of the $30 \times 30 \times 30$ one) roughly maintains the polymer concentration, but decreases the fiber-to-fiber distance. For Fréedericksz and saturation thresholds at $w = 1$ one now finds $\eta_F^{18} = 0.027 \pm 0.003$ and $\eta_s^{18} = 0.30 \pm 0.03$, respectively, where η is proportional to the square of the field strength. The corresponding thresholds for the larger $30 \times 30 \times 30$ sample are $\eta_F^{30} = 0.0085 \pm 0.0015$ and $\eta_s^{30} = 0.30 \pm 0.015$. From this data one can conclude that like in slab geometry (and for strong enough anchoring) the Fréedericksz threshold field strength scales approximately as

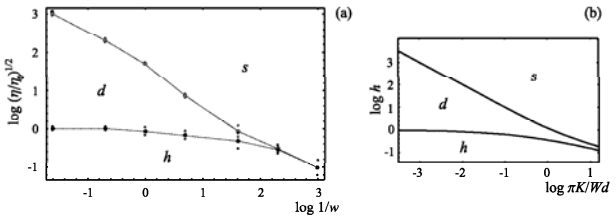

Figure 7. (a) Structural phase diagram $\log\sqrt{\eta/\eta_0}$ vs. $\log 1/w$ calculated for $T^* = 1.0$ and $R/a = 5$; η_0 corresponds to the Fréedericksz threshold at the strongest anchoring considered, $w = 5$. (b) Phase diagram for a nematic slab (from Ref. [20]) plotted in scales and ranges allowing for a comparison with (a). h denotes field strength values normalized with respect to the Fréedericksz threshold for infinite anchoring.

d_*^{-1}, if d_* is taken to be the shortest fiber-to-fiber distance. On the other hand, the saturation transition threshold remains almost unaltered.

2.2 Irregular fiber array

The actual topography of a polymer network shown in typical SEM pictures [3, 2] is much more complex than the regular array of straight and parallel fibers considered so far. In particular, the interfiber distance distribution is expected to play an important role in the switching process. Therefore, as a first step towards a more complex network topography, an irregular array of straight fibers has been studied, increasing the lattice size to $50 \times 50 \times 50$ particles and including 8 straight and parallel fibers of equal thickness, with $R = 3a$. The fibers were oriented along the z-axis, but distributed randomly within the xy-plane. The polymer concentration and fiber radii were kept unchanged in comparison with the previous $18 \times 18 \times 18$ case, yielding the same average fiber-to-fiber distance. Again, the external field was applied along the y-axis and the surface anchoring was assumed to be planar (with $w = 1$) along the z-axis. The concentration of the polymer (i.e., the percentage of ghost particles) was approximately 9%. In the following, the regular array sample (previous Section) will be referred to as "sample A", while the sample with the fiber position irregularity as "sample B". Moreover, "sample C" containing distorted fibers will be introduced later in this Section. Simulation runs involving samples of B and C-type consisted

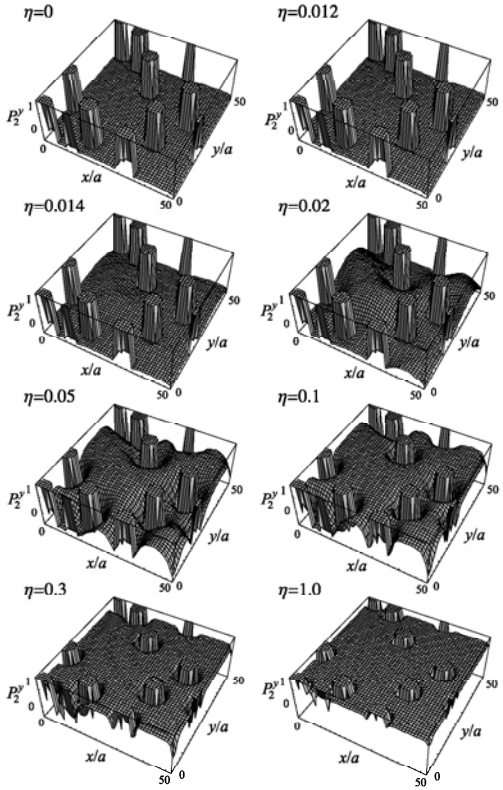

Figure 8. Array of several (8) straight fibers (sample B): $P_2^y(\mathbf{r}_i)$ order parameter map (xy cross section) for different η. The switching process is initiated approximately at $\eta_B = 0.013$. The "columns" represent parallel straight polymer fibers. Calculated for $T^* = 1.0$, $w = 1$, and $R/a = 3$.

of 8×10^4 equilibration and 6.6×10^4 production cycles, while for the smaller A-type sample the equilibration run was shortened to 6×10^4 cycles.

Fig. 8 shows the evolution of the local P_2^y averaged over MC cycles for every particle within a given xy-cross section for sample B. For $\eta < 0.012$ one has $P_2^y(\mathbf{r}_i) \approx -0.3$ constant and negative, showing that particles are still aligned along $\mathbf{z}$ (recall that at $T^* = 1.0$ one has $S \approx 0.6$) and that the Fréedericksz threshold has not been reached yet. Reaching, however, $\eta = 0.014$, in regions where the fiber density is below average (the interfiber distance above average), the particles start to reorient along the field direction and P_2^y increases, becoming even positive in some areas upon a further increase in η. It is important to notice that now the Fréedericksz threshold is significantly lower than in the regular array case with the same polymer concentration — sample A. This can be attributed to the fact that the external field always destabilizes the longest-wavelength distortion first. Then, unlike in sample A, in the irregular sample B there is a distribution of effective fiber-to-fiber distances, allowing also for deformations whose wavelength is larger than the average interfiber distance. As the field strength is increased even further, the parallel-to-fiber alignment persists only in the very vicinity of fibers and P_2^y becomes positive almost everywhere. Finally, for extremely strong fields the saturation threshold is reached as well, and then all molecules are aligned along the external field direction. In addition, the strong field enhances the degree of nematic order [21]. Note that the switching of the molecular orientation has not occurred in all parts of the sample simultaneously. Indeed, very strong fields are required to switch the particle orientation in polymer-rich regions (see Fig. 8, for $\eta \leq 0.3$, in the left corner). Consequently, the Fréedericksz transition is not as sudden as in a regular array-system. The saturation transition, on the other hand, is driven merely by a competition between surface anchoring and the external field, and is not significantly affected by the positional irregularity of the network.

The last step in modeling the polymer network topography consisted of dropping the assumption that the fibers be straight and parallel and considering a system of distorted fibers instead. Again, the general (average) fiber direction was taken along the z-axis. Then each of the fibers (whose thickness was assumed constant along z) was generated by performing a biased random walk resulting in the structure shown in Fig. 9, "sample C". Surface anchoring was assumed planar, here, however, along the local fiber direction (not necessarily matching with the z-direction), with $w = 1$. The second-rank order parameter for ghost particles $\langle P_2 \rangle_g$

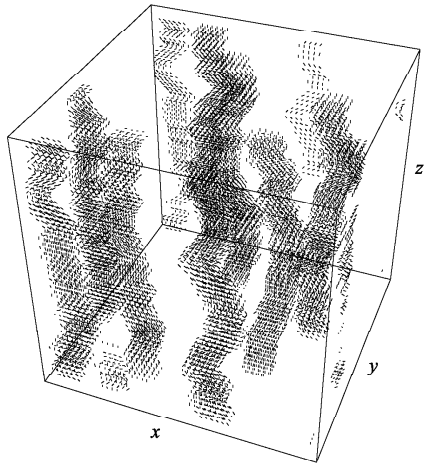

Figure 9. Array of several distorted fibers (sample C): ghost particles representing the fixed polymer fiber network; $\langle P_2 \rangle_g \approx 0.28$.

(see Section 1.1) represents a measure of fiber distortion. For sample C $\langle P_2 \rangle_g \approx 0.28$.

The switching process was simulated also for the sample C. It turns out that despite fiber distortions, in absence of external fields ($\eta = 0$) the net molecular orientation seems to be still well-defined (along the average fiber direction, z-axis), except for the fiber vicinity where it is affected by the local anchoring easy axis. Due to network irregularity the external field and the anchoring easy axis are never strictly perpendicular to each other, therefore — unlike in Fréedericksz geometry, samples A and B — the external field torque acts on nematic particles already at arbitrarily low field strengths. As we shall see later, this results in a decrease of the field threshold value in comparison to more regular samples A and B, while the switching itself is relatively sudden. At the same time it should be kept in mind that the sample C studied here covers length scales up to 0.25 μm (depending on the choice for a; usually 1 nm $\leq a \leq$ 5 nm), i.e., still far below macroscopic dimensions. As a consequence, the detailed

switching behavior depends sensitively on the specific irregularities of the network generated for sample C.

2.3 Experimental observables and network irregularity

For the switching in a symmetry-lacking sample it is instructive to explore simulation-predicted experimental observables, rather than study specific order parameter maps. Therefore, this Section will be devoted to the analysis of selected experimental observables (electric capacitance [3], intensity of transmitted polarized light, and ^{2}H NMR spectra), along with a comparison of samples A, B, and C. As these methods all monitor the bulk response of the system, they are suitable for monitoring the Fréedericksz transition, but are rather insensitive to the saturation transition.

The electric capacitance measurements rely on the orientational anisotropy of the molecular dielectric constant, leading to changes in sample capacitance for any major molecular reorientation. Simulating capacitance, it was assumed that the probing electric field is — like the aligning external field $\mathbf{f}$ — directed strictly along the y-axis throughout the sample, but is, unlike the external field, not homogeneous. In absence of free ions and provided, moreover, that molecular ordering is mostly restricted to the yz-plane and that elastic deformations within the xz-plane are weak, the effective static capacitance for a $M \times M \times M$ sample can be calculated as [3, 12]

$$C_y = \epsilon_0 \sum_{k=1}^{M} \sum_{l=1}^{M} \left(\sum_{m=1}^{M} \frac{1}{\epsilon(k,l,m)} \right)^{-1}, \qquad (4)$$

where the indices k, l, and m run along the x, z, and y coordinates, respectively. Here we consider that each group of molecules represented by $\mathbf{u}_i$ and located at (k,l,m) is endowed with a local dielectric constant $\epsilon(k,l,m) = \epsilon_\perp + (\epsilon_\parallel - \epsilon_\perp)(\mathbf{u}_i \cdot \mathbf{f})^2$.

The calculations were performed for $\epsilon_\parallel = 29.8$ and $\epsilon_\perp = 6.1$, assuming as in Ref. [3] the same dielectric anisotropy for the polymer network. The C_y versus η characteristics for three samples (A, B, and C) with $R/a = 3$ and same polymer concentration ($\approx 9\%$), but different network topography, is shown in Fig. 10. In Fréedericksz-like geometry where the external field is strictly perpendicular to fibers (samples A and B), the orientational transition happens abruptly at a well-defined threshold (η_A and η_B, respectively, with $\eta_A > \eta_B$). In sample C network irregularities further decrease the switching threshold (η_C; not well-defined anymore), yet keep the reorientational process relatively sudden. The thresholds for

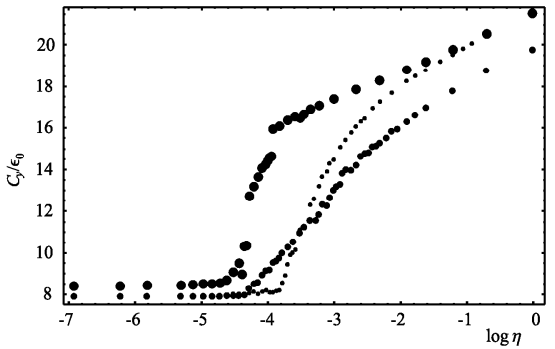

Figure 10. External field-induced switching as monitored by capacitance (C_y) measurements: sample A (small dots), sample B (medium dots), and sample C (large dots).

the three samples can from Fig. 10 be identified as $\eta_A = 0.022 \pm 0.001$, $\eta_B = 0.013 \pm 0.001$, and $\eta_C = 0.010 \pm 0.002$, with $\eta_C < \eta_B < \eta_A$, as expected. Note that the $C_y(\eta)$ curve is most gradual for sample B because molecules in polymer-rich sample regions refuse to switch unless the field is extremely strong. Further, the increase of C_y for large η is to be attributed to enhanced nematic order rather than to particle reorientation.

Another convenient method for the determination of the Fréedericksz threshold are the measurements of the intensity of polarized light transmitted through the sample [22]. Let again the average fiber direction coincide with the z-axis and let the external field be applied along the y-axis, with the light beam also propagating in this direction. In a nematic slab of thickness d with planar anchoring along z (and with no polymer networks) there is no x or z-dependence in the director field. The intensity of light transmitted through such a sample (if put between two polarizers crossed at a right angle) is given by the formula

$$I = I_0 \sin^2(2\varphi_0) \sin^2(\Delta\Phi/2), \qquad (5)$$

with I_0 denoting the intensity of the incoming polarized light. Further, $\Delta\Phi$ — also called birefringence — is the phase difference between the ordinary and extraordinary ray (characterized by refractive indices n_o and

n_e, respectively) accumulated upon passing through the sample. The output signal is maximized when the angle φ_0 between the projection of the director onto the xz-plane and the incident light polarization plane is equal to $\pi/4$. Having fixed φ_0, the output signal I depends only on the birefringence $\Delta\Phi = (2\pi/\lambda)\int_0^d |n_e(y) - n_o| dy$, i.e., $I \propto \sin^2(\Delta\Phi/2)$. This implies that I is constant below the Fréedericksz threshold, but shows oscillatory behavior above it. The total number of oscillations seen upon increasing the field strength is approximated by $\Delta n^0 Sd/\lambda$, where Δn^0 stands for the maximum difference of indices n_e and n_o in a perfectly ordered nematic where $S = 1$. From such a graph, the Fréedericksz threshold can be estimated by identifying the point where the $I(\eta)$ curve begins to oscillate (as in Ref. [22]).

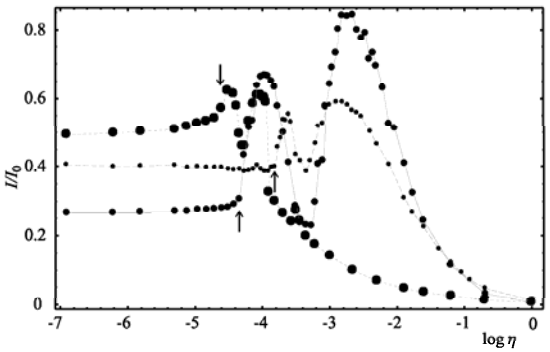

Figure 11. External field-induced switching as monitored by transmitted polarized light intensity (I) measurements: sample A (small dots), sample B (medium dots), and sample C (large dots). The arrows indicate switching thresholds as determined from the capacitance measurement (Fig. 10).

Simulating switching in nematic samples with dispersed polymer networks, the incoming light polarization plane was fixed at $\varphi_0 = \pi/4$. The sample thickness for the optics calculation was set to 10 μm by allowing for several light passes through the sample before measuring the transmitted intensity. Within each "pixel" in the xz-plane polarized light was propagated along the y-axis using the Jones matrix formalism, assuming that the local and instantaneous optical axes are given by $\mathbf{u}_i$. Since the inhomogeneity length scale within the xz-plane is much

smaller than the light wavelength λ, the transmitted intensity $I(x, z)$ was averaged over pixels within the light beam cross section. Both light scattering and diffraction have been neglected [2]. Further, it was assumed that the polymer network is optically isotropic, with a refractive index $n_p = 1.499$, while for the perfectly ordered nematic the corresponding indices were set to $n_e = 1.7445$ (maximum value) and $n_o = 1.520$. Probing such a sample with He-Ne laser light with $\lambda = 632.8$ nm, at $T^* = 1.0$ with $S \approx 0.6$ the birefringence can be estimated as $2\pi \times 2.1$. Consequently, two oscillations can be anticipated in the $I(\eta)$-dependence. Inspecting the simulated $I(\eta)$ curves shown in Fig. 11, one immediately recognizes the oscillatory behavior predicted above. Again, curves for samples A, B, and C are characterized by different Fréedericksz thresholds, matching with those observed already in the capacitance measurement. Moreover, the oscillations of I are slowest for sample B, which is in agreement with the lowest slope of the $C_u(\eta)$ capacitance curve (Fig. 10). At extremely strong fields no light is transmitted because the birefringence approaches zero.

Finally, we inspect the ^{2}H NMR spectra calculated to monitor the switching process. Fig. 12 comparatively shows the spectra calculated for samples A, B, and C, with the spectrometer field applied along the (average) fiber direction, z-axis. Again, a smoothening convolution with a Lorentzian kernel of width $\approx 0.07\,\delta\omega_Q$ was performed and translational diffusion was assumed, with the same (fast) diffusion rate as in Section 1.1. Consider sample A first. In absence of the external field, as well as for low η, in the spectrum there are two well-defined lines positioned approximately at a maximum frequency splitting reduced by a factor of $S \approx 0.6$. This is a signature of fiber-imposed molecular ordering along z below the Fréedericksz threshold. Once the threshold at $\eta_A \approx 0.022$ is reached, molecular orientations start to switch along the external field direction (perpendicular to the spectrometer field), and the splitting is reduced. At very high fields already above the saturation transition the quadrupolar splitting should equal half the splitting observed at zero field, provided that the degree of ordering remains unchanged. In a strong external field, however, this never is the case and therefore the splitting keeps on increasing as the field becomes stronger. Moving to sample B, one can observe that the low-field splitting starts to decrease already at $\eta_B \approx 0.013$. Moreover, the switching process is also more gradual, which is all in agreement the other two experiments. In sample C at low fields one also finds a double-peaked line shape, yet at a splitting slightly lower than in the previous two cases. This indicates that despite the network being highly irregular, the z-orientation of molecules is still maintained in most of the sample, except for the

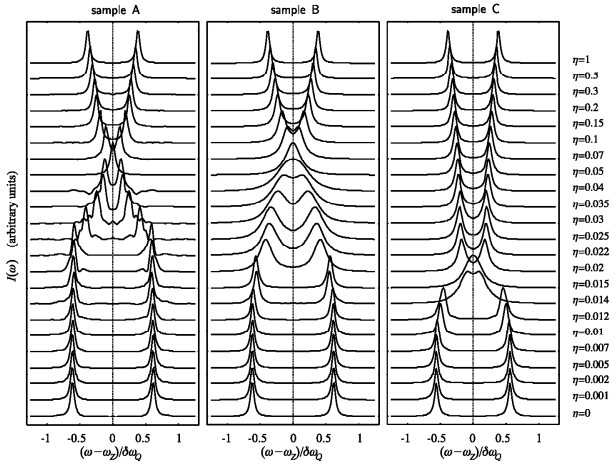

Figure 12. External field-induced switching as monitored by ^{2}H NMR spectra: sample A (*left*), sample B (*center*), and sample C (*right*). In all cases $T^* = 1$ and $w = 1$. The spectra of sample A show more noise because this sample contains 5256 particles only — as opposed to 112200 particles in samples B and C.

closest distance from the distorted fibers. Note also that the sample C switches already at $\eta_C \approx 0.010$, which, again, is the lowest threshold of all. In addition, the switching is more sudden than in sample B.

3. Pretransitional ordering in the isotropic phase

The last issue considered in this Chapter will be pretransitional ordering in a nematic sample with dispersed polymer networks above the NI transition ($T^*_{NI} = 1.1232$). As seen already in studying a regular fiber array, some surface-induced paranematic ordering may persist in the vicinity of fibers. This ordering can be detected by optical means [2]; alternatively, it can be detected also by ^{2}H NMR [23].

The simulations presented in this Section were all performed with sample C presented in Section 1.2.3 (see Fig. 9). Again, planar anchoring along the local fiber direction was assumed and there was no external field applied. Paranematic ordering can then be characterized by a director parallel to the local fiber direction, and by a degree of order S decaying from a nonzero surface value to $S \approx 0$ over $\xi \approx 5a$ (at $T^* = 1.2$), the corresponding correlation length. Therefore, in a low-polymer-density sample areas with $S \neq 0$ are limited only to the very vicinity of fibers. In high-polymer-density samples, on the other hand, fibers can approach each other (or even cross-link) and thereby create "bridges" of nematic order with $S \neq 0$ wherever the lowest fiber-to-fiber distance becomes comparable to $\approx 2\xi$ — see Fig. 13. This effect is similar to the capillary condensation observed experimentally in thin nematic films by force spectroscopy [24], potentially allowing for a self-assembly of colloidal particles. The actual degree of paranematic order depends significantly also on temperature (T^*) and on the strength of the orientational coupling of the liquid crystal with the fiber surface (w). Therefore, in this Section simulation results for different T^* and w will be presented, focusing on the experimental output: transmitted light intensity and ^{2}H NMR line shapes. In the simulation, the sample was equilibrated during 8×10^4 MC cycles and, afterwards, 7×10^4 cycles were used to accumulate the relevant observables.

The set-up of the optical experiment was identical to that used in Section 1.2.3: net fiber direction along the z-axis, light beam along the y-axis, and the polarizer and analyzer crossed in the xz-plane, each of them at an angle of $\pi/4$ with respect to the z-axis. Further, same sample thickness and light wavelength were considered. Again, the polymer was assumed optically isotropic and the refractive indices of the liquid crystal equal to those used in Section 1.2.3. As already discussed, the intensity of outcoming light I is proportional to $\sin^2(\Delta\Phi/2)$, where the effective birefringence $\Delta\Phi$ is proportional to the difference between the extraordinary (n_e) and ordinary (n_o) refraction index averaged along the path of the light beam. Assuming that the net direction of paranematic ordering — averaged over the whole sample — still coincides with the z-axis, as imposed by the polymer network, and that $n_e - n_o$ is small in comparison with n_e and n_o, $\Delta\Phi$ is simply proportional to the overall degree of order, in this case given by $\langle P_2^z \rangle$. Note that the averaging performed to calculate $\Delta\Phi$ has to be carried out both over local rapid fluctuations of molecular long axes (defining the local standard nematic order parameter S), and across the sample over changes in the local director and polymer fiber orientations (characterized by the $\langle P_2 \rangle_g$ order parameter). Following the addition theorem for spherical harmonics and performing all averages (neglecting biaxiality), one can approximately

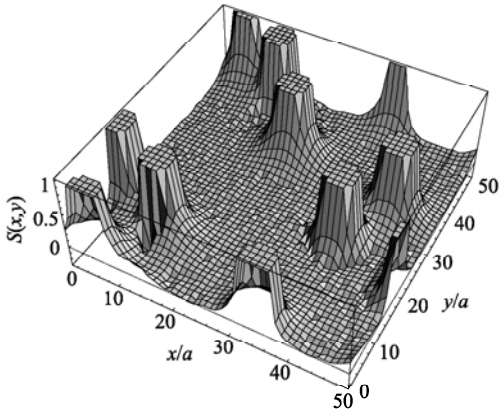

Figure 13. Pretransitional ordering in sample C at $T^* = 1.2$, for planar anchoring with $w = 1$: $S(x, y)$ order parameter map cross section at $z/a = 25$. The paranematic order decays to zero over the correlation length $\xi \approx 5a$, except in polymer-rich areas where nematic "bridges" can form in between fibers (as here in the left lower corner with $S \leq 0.2$). Note that while the "columns" denoting fiber positions are vertical (with $S = 1$), the fibers themselves can be tilted with respect to the xy-plane (Fig. 9).

write $\langle P_2^z \rangle = \langle S \rangle \langle P_2 \rangle_g$, where $\langle S \rangle$ is the spatial average of S. Hence, $\Delta\Phi \propto \langle S \rangle$ [2].

Fig. 14 shows the simulated transmitted light intensity (I) curves versus reduced temperature (above $T^*_{NI} = 1.1232$) for different anchoring strengths w. As expected, the intensity I is nonzero due to paranematic surface-induced ordering, $\langle S \rangle \neq 0$, and decreases with increasing T^*. Curves in Fig. 14 are similar to the corresponding experimental ones plotted in Ref. [2]. Note, however, that the increase of I/I_0 on approaching T^*_{NI} from above is not as abrupt as in Ref. [2]. This may be because in the present simulation the NI transition was not approached as closely as in the experiment. Further, in the present study I/I_0 is well-behaved also because the effective birefringence is not necessarily small — the polymer network is rather dense and $\Delta\Phi \ll 1$ does not always hold (e.g., for $w = 1$) — and any significant variation of $\Delta\Phi$ is saturated in the $I \propto \sin^2(\Delta\Phi/2)$ dependence. For the same reason, the curve for $w = 1$ is not monotonous close to the NI transition. With

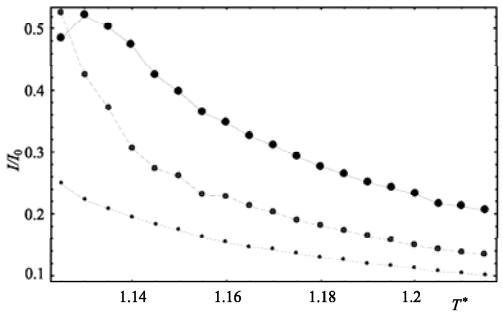

Figure 14. Pretransitional ordering: transmitted polarized light intensity I as a function of T^* for different anchoring strengths: $w = 1$ (large dots), $w = 0.5$ (medium dots), and $w = 0.1$ (small dots). I_0 denotes the intensity of the incoming light.

decreasing anchoring strength w the degree of ordering decreases, which then translates into a lower I/I_0 signal.

Alternatively, pretransitional ordering can be detected also via ^{2}H NMR. The quadrupolar line splitting depends both on the local orientation of the nematic director (matching with the local orientation of the fiber network) and on the local degree of order. The spectra presented in Fig. 15 were calculated for sample C in the fast diffusion limit (the rate of diffusion being 1024 diffusive steps per NMR cycle, as earlier in this Chapter), with the spectrometer magnetic field directed along the z-axis. In this case the spectrum consists of one or two well-defined lines positioned at an average frequency $\omega_Z \pm \langle \omega_Q(\mathbf{r}) \rangle$, where $\langle ... \rangle$ stands for the spatial average. As above, in case of predominantly uniaxial molecular ordering the spherical harmonics addition theorem can be applied to the expression for quadrupolar splitting when $\langle \omega_Q(\mathbf{r}) \rangle$ is calculated, resulting in $\langle \omega_Q(\mathbf{r}) \rangle = \delta\omega_Q \langle S \rangle \langle P_2 \rangle_g$.

Fig. 15 shows the evolution of ^{2}H NMR spectra upon increasing T^* for different values of the anchoring strength w. A convolution of the spectra with a Lorentzian kernel of width $\approx 0.07\,\delta\omega_Q$ was performed in order to smoothen the spectra. The left sequence of spectra in Fig. 15 is plotted for $w = 1$ where the surface degree of order is high enough to yield a double-peaked spectrum. For $T^* = 1.2$ the peak is estimated to be located at $|\omega_Q/\delta\omega_Q| \approx 0.04 \pm 0.01$. On the other hand, $\langle S \rangle \langle P_2 \rangle_g$

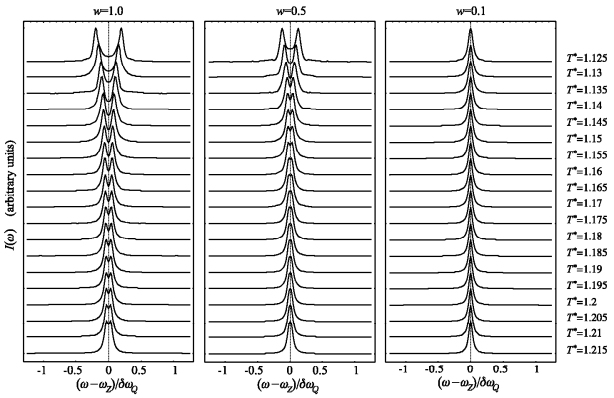

Figure 15. Pretransitional ordering: diffusion-averaged ^{2}H NMR spectra as a function of T^* for different anchoring strengths: $w = 0.1$ (*left*), $w = 0.5$ (*center*), and $w = 0.1$ (*right*). Double-peaked line shapes are a signature of surface-induced paranematic ordering.

gives ≈ 0.036, and hence the agreement of the two estimates is reasonably good. When decreasing the temperature towards T^*_{NI}, the effective quadrupolar splitting increases, which results from an increase of $\langle S \rangle$. For weaker anchoring ($w = 0.5$ and $w = 0.1$) the overall $\langle S \rangle$ is smaller and the calculated spectra are only single-peaked — except rather close to T^*_{NI} for $w = 0.5$ — because of their finite resolution.

4. Conclusions

In conclusion, the simulations based on simple Lebwohl-Lasher modeling can reproduce the qualitative behavior of the composite liquid crystal-polymer network system. The polymer fibrils seem to be able to align the surrounding liquid crystal despite partial orientational disorder at the surface. For homeotropic anchoring conditions on the fiber surface topological defects in nematic ordering are observed. Further, the switching performance in an external field depends on the positional order of the fibers and their distortion: systems of straight and parallel fibers with a broad interfiber distance distribution give a gradual

switching, while in a system of distorted fibers this process is much more sudden. Finally, above the nematic-isotropic transition temperature paranematic ordering can be observed in the system. All these conclusions can be drawn by inspecting the simulated experimental observables.

Acknowledgments

The authors wish to thank EU through TMR FULCE "*Functional Liquid–Crystalline Elastomers*", contract HPRN-CT-2002-00169, for financial support.

References

[1] G. P. Crawford and S. Žumer, *Liquid Crystals in Complex Geometries Formed by Polymer and Porous Networks*, Taylor and Francis, London (1996).

[2] Y. K. Fung, A. Borštnik, S. Žumer, D.-K. Yang, and J. W. Doane, *Phys. Rev. E*, 55:1637 (1997).

[3] R.-Q. Ma and D.-K. Yang, *Phys. Rev. E*, 61:1567 (2000).

[4] M. J. Escuti, C. C. Bowley, G. P. Crawford, and S. Žumer, *Appl. Phys. Lett.*, 75:3264 (1999).

[5] I. Dierking, L. L. Kosbar, A. Afzali-Ardakani, A. C. Lowe, and G. A. Held, *Appl. Phys. Lett.*, 71:2454 (1997).

[6] I. Dierking, L. L. Kosbar, A. C. Lowe, and G. A. Held, *Liq. Cryst.*, 24:397 (1998); *Liq. Cryst.*, 24:387 (1998).

[7] P. A. Lebwohl and G. Lasher, *Phys. Rev. A*, 6:426 (1972).

[8] C. Chiccoli, P. Pasini, G. Skačej, C. Zannoni, and S. Žumer, *Phys. Rev. E*, 65:051703 (2002).

[9] D. Andrienko, M. P. Allen, G. Skačej, and S. Žumer, *Phys. Rev. E*, 65:041702 (2002).

[10] N. Schopohl and T. J. Sluckin, *Phys. Rev. Lett.*, 59:2582 (1987).

[11] A. Sonnet, A. Killian, and S. Hess, *Phys. Rev. E*, 52:718 (1995).

[12] C. Chiccoli, P. Pasini, G. Skačej, C. Zannoni, and S. Žumer, *Phys. Rev. E*, 67:010701(R) (2003).

[13] N. Metropolis, A. W. Rosenbluth, M. N. Rosenbluth, A. H. Teller, and E. Teller, *J. Chem. Phys.*, 21:1087 (1953).

[14] J. A. Barker and R. O. Watts, *Chem. Phys. Lett.*, 3:144 (1969).

[15] P. Pasini and C. Zannoni, *Advances in the Computer Simulations of Liquid Crystals*, Kluwer, Dordrecht (2000).

[16] U. Fabbri and C. Zannoni, *Mol. Phys.*, 58:763 (1986).

[17] P. G. de Gennes and J. Prost, *The Physics of Liquid Crystals*, Clarendon Press, Oxford (1993).

[18] P. M. Chaikin and T. C. Lubensky, *Principles of Condensed Matter Physics*, Cambridge University Press, Cambridge (1997).

[19] C. Chiccoli, P. Pasini, G. Skačej, C. Zannoni, and S. Žumer, *Phys. Rev. E*, 60:4219 (1999); *Phys. Rev. E*, 62:3766 (2000).

[20] J. Nehring, A. R. Kmetz, and T. J. Scheffer, *J. Appl. Phys.*, 47:850 (1976).

[21] I. Lelidis, M. Nobili, and G. Durand, *Phys. Rev. E*, 48:3818 (1993).

[22] H. Gruler, T. J. Scheffer, and G. Meyer, *Z. Naturforsch. A*, 27:966 (1972).

[23] A. Golemme, S. Žumer, D. W. Allender, and J. W. Doane, *Phys. Rev. Lett.*, 61:2937 (1988).

[24] K. Kočevar, A. Borštnik, I. Muševič, and S. Žumer, *Phys. Rev. Lett.*, 86:5914 (2001).